

RESEARCH ARTICLE

10.1002/2015JD023813

Key Points:

- Sensible heat flux (SHF) impacts on cold pool dissipation are investigated
- Turbulent entrainment is an important mechanism for dissipation
- Prescribed and bulk SHF formulations have different effects on cold pools

Correspondence to:

L. D. Grant,
ldgrant@atmos.colostate.edu

Citation:

Grant, L. D., and S. C. van den Heever (2016), Cold pool dissipation, *J. Geophys. Res. Atmos.*, 121, 1138–1155, doi:10.1002/2015JD023813.

Received 16 JUN 2015

Accepted 2 JAN 2016

Accepted article online 7 JAN 2016

Published online 6 FEB 2016

Cold pool dissipation

Leah D. Grant¹ and Susan C. van den Heever¹¹Department of Atmospheric Science, Colorado State University, Fort Collins, Colorado, USA

Abstract The mechanisms by which sensible heat fluxes (SHFs) alter cold pool characteristics and dissipation rates are investigated in this study using idealized two-dimensional numerical simulations and an environment representative of daytime, dry, continental conditions. Simulations are performed with no SHFs, SHFs calculated using a bulk formula, and constant SHFs for model resolutions with horizontal (vertical) grid spacings ranging from 50 m (25 m) to 400 m (200 m). In the highest resolution simulations, turbulent entrainment of environmental air into the cold pool is an important mechanism for dissipation in the absence of SHFs. Including SHFs enhances cold pool dissipation rates, but the processes responsible for the enhanced dissipation differ depending on the SHF formulation. The bulk SHFs increase the near-surface cold pool temperatures, but their effects on the overall cold pool characteristics are small, while the constant SHFs influence the near-surface environmental stability and the turbulent entrainment rates into the cold pool. The changes to the entrainment rates are found to be the most significant of the SHF effects on cold pool dissipation. SHFs may also influence the timing of cold pool-induced convective initiation by altering the environmental stability and the cold pool intensity. As the model resolution is coarsened, cold pool dissipation is found to be less sensitive to SHFs. Furthermore, the coarser resolution simulations not only poorly but sometimes wrongly represent the SHF impacts on the cold pools. Recommendations are made regarding simulating the interaction of cold pools with convection and the land surface in cloud-resolving models.

1. Introduction

In the Aqua Moderate Resolution Imaging Spectroradiometer (MODIS) true color image over the Sahara desert shown in Figure 1, both young and mature cold pools generated by latent cooling associated with precipitation, and their associated outflow boundaries or gust fronts, are apparent from the shallow cloud features that form along their leading edges. Cold pools are common over the Sahara, and they have been shown to play important roles in dust lofting and in the climatology of dry continental regions [e.g., Miller *et al.*, 2008; Garcia-Carreras *et al.*, 2013]. The most prominent outflow boundary in Figure 1 (indicated by the lower arrow) has spread laterally away from its parent convective storm and is serving as a focal point for new convective development along its northernmost periphery. Although it is widely known that cold pools may initiate convection, several questions arise regarding the details depicted in Figure 1. Is the rate of dissipation of the cold pool important in determining the temporal and spatial scales over which cold pools can initiate convection? What processes are responsible for cold pool dissipation? What role do surface sensible heat fluxes, which are large over dry land surfaces such as the Sahara, play in this dissipation? In this study, we explore several aspects pertinent to these broader questions.

Cold pool outflows play important roles in the organization and structure of clouds and cloud systems on all scales, from trade cumulus [e.g., Rauber *et al.*, 2007; Zuidema *et al.*, 2012] and stratocumulus [e.g., Wood *et al.*, 2011; Terai and Wood, 2013] to deep convection [e.g., Rotunno *et al.*, 1988; Tompkins, 2001, hereafter T01; Khairoutdinov and Randall, 2006]. As discussed above, cold pools can initiate deep convection, providing a lifting or triggering mechanism on their own or through their interaction with mesoscale boundaries such as sea breezes [e.g., Kingsmill, 1995; Carbone *et al.*, 2000; Grant and van den Heever, 2014] and other gust fronts [e.g., Purdom, 1982; Droegemeier and Wilhelmson, 1985; Wilson and Schreiber, 1986].

Idealized modeling simulations have been instrumental in advancing our understanding of varying aspects of cold pool, or density current, characteristics. These modeling studies have examined the turbulent and dynamic characteristics of density currents and the impact of the environment, such as the background stability and shear, on the cold pool dynamics [e.g., Droegemeier and Wilhelmson, 1987, hereafter DW87; Xu, 1992; Liu and Moncrieff, 2000, hereafter LM00; Seigel and van den Heever, 2012, hereafter SvdH12; Bryan and Rotunno, 2014; Rooney, 2015]. Other studies have examined the role of microphysical processes and

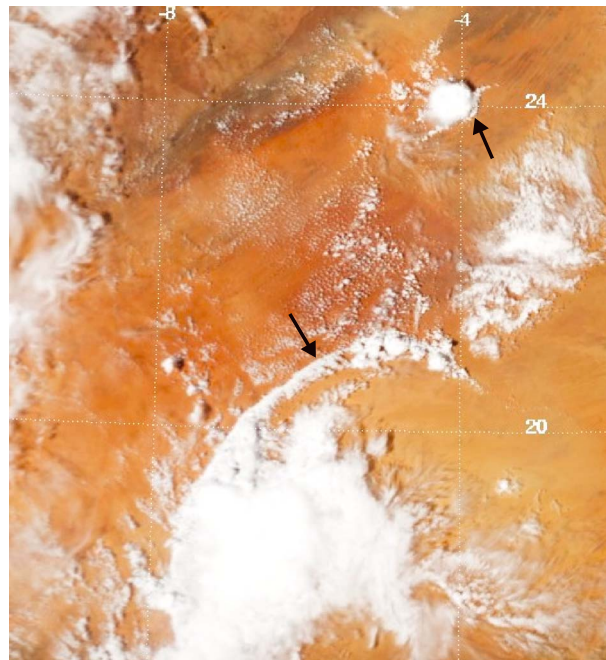


Figure 1. Aqua MODIS true color scene over the northwestern Sahara desert at 1330 UTC 4 September 2010. Outflow boundaries are denoted by arrows.

the subsequent thermodynamic characteristics of cold pools [e.g., Gilmore *et al.*, 2004; van den Heever and Cotton, 2004; Dawson *et al.*, 2010]. However, relatively few studies have quantitatively investigated the impact of surface energy fluxes on density currents, although both observational and cloud-resolving modeling studies have documented enhancements in surface sensible heat fluxes (SHFs) and latent heat fluxes (LHFs) within cold pools over tropical oceanic regions [Johnson and Nicholls, 1983; Young *et al.*, 1995; Jabouille *et al.*, 1996]. T01 suggested that the enhanced surface fluxes within the cold pool are important for cold pool dissipation time and convective initiation in tropical oceanic conditions. (The term “cold pool recovery” has been previously used in the literature, including in T01. However, we opt instead to use the term “dissipation” when referring to the weakening of the cold pool itself. The term “recovery” is more

appropriate when referring to the evolution of the environment to precold pool conditions.) To date, little to no data exist documenting surface fluxes within cold pools over land.

Surface energy fluxes may impact cold pool dissipation through two mechanisms: by (a) enhancing turbulence and entrainment of environmental air into the cold pool and (b) directly modifying the cold pool buoyancy. Linden and Simpson [1986] studied mechanism (a) within laboratory experiments by producing bubbles that disrupted the gravity current front. Ross *et al.* [2004] investigated mechanism (b) utilizing both an integral model and a shallow water model that represented tropical oceanic conditions and neglected entrainment. These studies suggested that both effects could be important. However, an investigation of cold pool sensitivity to surface fluxes at a physical process level using more sophisticated numerical models is still lacking. Additionally, the specific role of SHFs separate from LHFs has not yet been considered, with the possible exception of Linden and Simpson's [1986] laboratory study. Rooney [2015] recently highlighted the need to investigate the impact of SHFs on cold pool behavior.

The focus of this study is on the particular role of SHFs. We address the hypothesis that cold pool characteristics, including cold pool temperature, vertical velocity above the cold pool head, and propagation speed, are sensitive to SHFs. Classical density current arguments [e.g., Benjamin, 1968] suggest that cold pools should dissipate more quickly, and hence have weaker vertical velocities associated with the head circulation and slower propagation speeds, when SHFs are included compared to when they are not. We investigate this hypothesis using an idealized two-dimensional (2-D) numerical modeling framework and an environment representative of daytime, arid, continental conditions (e.g., Figure 1); water vapor and hence LHFs are excluded to isolate the impacts of SHFs. Specifically, the role of SHFs in modifying cold pool characteristics is investigated under the following scenarios: (1) bulk fluxes that depend on the wind speed and air-surface temperature difference assuming a fixed surface temperature and specified constant fluxes and (2) a range of model resolutions. As will be shown, the bulk fluxes only occur within the cold pool and therefore represent direct modification of the cold pool buoyancy by SHFs (i.e., mechanism (b) above), while the constant SHFs do not heat the cold pool *relative* to the environment (the flux is constant across the domain) and therefore represent the indirect effects of SHFs on turbulent entrainment into the cold pool (i.e., mechanism (a) above). These two sets of scenarios are also tested in order to evaluate the extent to which the choices of SHF formulation and model resolution matter for simulating SHF impacts on cold pools.

2. Methods

2.1. Model Description

A 2-D, nonhydrostatic, quasi-compressible model was utilized for these experiments. The 2-D simulation setup, which has been used in many previous idealized simulations of density currents, was chosen in order to facilitate the large number of simulations necessary (128 total). A disadvantage of using 2-D is that the turbulent energy cascade is not properly represented; the implications of this assumption will be discussed in the subsequent sections. As discussed in section 1, water vapor is not included in any of the experiments presented here, thus facilitating our focus on SHFs. Four prognostic equations for u (zonal wind, m s^{-1}), w (vertical wind, m s^{-1}), θ' (potential temperature, K, where the prime denotes a perturbation from the base state which is only a function of height), and π' (perturbation Exner function) are discretized in flux form on the Arakawa-C grid [Wilhelmson and Chen, 1982; DW87]. The equations and numerical methods utilized are the same as in SvdH12.

All simulations presented in this study were 800 km across and 15 km deep and were integrated for 4000 s. Additionally, a neutrally stratified, isentropic base state with a constant potential temperature of 300 K was utilized, and no initial winds were included. This allows for the investigation of cold pool dissipation under varying SHF formulations in simple background environmental conditions without the complicating effects of wind shear and vertically propagating or ducted gravity waves that may interact with the cold pool. The horizontal domain was long enough such that the cold pool was not influenced by the periodic lateral boundary conditions throughout the duration of the simulation, and the high domain top of 15 km has been used in previous studies of density currents propagating in an isentropic atmosphere [LM00]. The exclusion of moisture and the utilization of a neutrally stratified atmosphere is representative of a cold pool occurring in the afternoon over a relatively dry land surface when the boundary layer is deep and well mixed, such as those shown over the Sahara shown in Figure 1. By excluding water vapor, we neglect its contribution to buoyancy, which is typically much smaller than that of temperature perturbations. We also neglect any feedbacks to the cold pool by microphysical processes and precipitation formation, thereby simplifying the analysis.

In the highest resolution experiments, the horizontal (Δx) and vertical grid spacings (Δz) were 50 m and 25 m, respectively, and the time step (Δt) was 0.05 s (Table 1). The diffusion coefficients for the momentum variables were set to $25 \text{ m}^2 \text{ s}^{-1}$ and $12.5 \text{ m}^2 \text{ s}^{-1}$ in the horizontal and vertical directions, respectively, and were 3 times larger for the scalars [e.g., Deardorff, 1972; Klemp and Wilhelmson, 1978]. These values were determined to be the minimum necessary in order to reduce numerical noise and were held constant in space and time. A cosine-shaped cold bubble, the configuration and amplitude of which was varied in a suite of sensitivity experiments (described in section 2.2), was placed in the center of the domain at the initial time in order to initialize the density current, which will simply be called the cold pool from here on. The cold bubble was not maintained after the initial time. The grid setup and cold pool initialization were chosen in order to be consistent with previous idealized modeling studies of density currents [e.g., DW87; Straka et al., 1993; Liu and Moncrieff, 1996, LM00; SvdH12].

2.2. Sensitivity Experiments

As described in section 1, the influence of both bulk and constant SHF formulations was tested to elucidate the different mechanisms by which SHFs can contribute to cold pool dissipation. First, SHFs were excluded; these experiments are named “NoSHF.” For the set of bulk SHF experiments (“BulkSHF”), a bulk formula depending on the surface-air temperature difference and wind speed was implemented [e.g., Johnson and Nicholls, 1983]

$$\text{SHF} = c_p \rho C_D U (\theta_{\text{sfc}} - \theta_{\text{air}}) \quad (1)$$

where U is the magnitude of the horizontal wind speed, θ_{air} the air temperature, and ρ the air density at the lowest model level above ground. θ_{sfc} is the initial surface temperature, which is set to the value from the base state θ profile (300 K) and is held constant throughout the simulation integration. These SHFs are one-way interactive because the land surface temperature does not respond to the atmosphere; the implications of this assumption are discussed in section 3.3. c_p is the heat capacity of dry air at constant pressure. C_D is an aerodynamic bulk transfer coefficient. In order to represent a fairly smooth land surface such as bare sand or soil, C_D was set to 1.5×10^{-3} [Hartmann, 1994]. Two sets of constant SHF experiments were then

Table 1. Experiment Names and Descriptions

<i>SHF Experiments</i>			
Name	Description		
NoSHF	SHFs excluded		
BulkSHF	SHFs calculated using a bulk formula, assuming fixed surface temperature		
ConsSHF-300	SHF of 300 W m^{-2} imposed uniformly throughout the domain		
ConsSHF-BulkAvg	SHF value, calculated by averaging the SHFs over the cold pool from the corresponding BulkSHF simulation, imposed uniformly throughout the domain		
<i>Resolution Experiments</i>			
Grid Setup			
Name	$\Delta x, \Delta z$	n_x, n_z^a	Δt
50 m	50 m, 25 m	16,000, 600	0.05 s
100 m	100 m, 50 m	8,000, 300	0.1 s
200 m	200 m, 100 m	4,000, 150	0.2 s
400 m	400 m, 200 m	2,000, 75	0.4 s
<i>Cold Bubble Initialization Experiments</i>			
Bubble Characteristics			
Name	Amplitude ^b	$\text{rad}_x, \text{rad}_z^c$	z_{cent}^d
SfcTall-15	−15 K	4 km, 6 km	0 km
SfcTall-10	−10 K		
SfcTall-5	−5 K		
SfcWide-15	−15 K	6 km, 4 km	0 km
SfcWide-10	−10 K		
SfcWide-5	−5 K		
ElevTall-15	−15 K	4 km, 3 km	3 km
ElevTall-10	−10 K		
ElevTall-5	−5 K		
ElevWide-15	−15 K	6 km, 2 km	2 km
ElevWide-10	−10 K		
ElevWide-5	−5 K		

^aNumber of grid points in the horizontal and vertical directions.
^b−10 K and −5 K bubble amplitude simulations were only performed for 50 m and 100 m resolution experiment sets.
^cHorizontal and vertical radii of initial cold bubble.
^dAltitude of the center of the initial cold bubble.

performed. For the first set, named “ConsSHF-300,” a single SHF value of 300 W m^{-2} was imposed throughout the domain for the duration of the simulation. This value is representative of peak daytime SHFs over a relatively dry land surface according to observations [Mallet *et al.*, 2009; Marsham *et al.*, 2013]. In the second set, constant SHF simulations with total energy input comparable to that of the BulkSHF experiments were performed. For these simulations (“ConsSHF-BulkAvg”), the constant SHF value was determined by averaging the SHFs from the BulkSHF experiments spatially over the cold pool and temporally between 600 and 4000 s. The SHF magnitudes imposed for the various ConsSHF-BulkAvg simulations range from 12.7 to 51.4 W m^{-2} in the highest resolution simulations (see Figure 4c). The four sets of SHF experiments are summarized in Table 1. The SHFs were switched on after 600 s of model simulation time, a suitable spin-up period as reported in other studies [LM00; SvdH12], so as to ensure that the changes in cold pool characteristics due to the SHF formulation are not attributable to the initialization time period before the cold pool is well formed.

The impact of SHFs on cold pool characteristics was also investigated for three different model resolutions. Δx , Δz , and Δt were progressively doubled from the highest resolution simulations while holding the domain size fixed. The finest and coarsest *horizontal* grid spacings used were 50 m and 400 m. The diffusion coefficients were also scaled linearly as the grid spacings were increased. The reason for this is twofold. First, the Smagorinsky [1963] turbulence formulation dictates that the diffusion coefficient K is proportional to $(\Delta x \Delta z)^{0.5}$. Therefore, if both Δx and Δz are doubled, K should also be doubled. Second, doubling the diffusion coefficients along with the time step and grid spacings ensures that the nondimensional computational smoothing rates in the horizontal

($K_x \Delta t / \Delta x^2$) and in the vertical ($K_z \Delta t / \Delta z^2$) remain the same across all of the model resolution experiments [DW87]. The various resolution experiments are referred to by their horizontal grid spacings (Table 1).

In order to obtain a large sample size and to ensure that the trends in cold pool characteristics are robust as the SHF formulation is varied, a variety of different cold bubble initialization configurations were also tested. Four different spatial bubble configurations were used, two of which were centered at the surface and hence were dome shaped (bubbles SfcTall and SfcWide; Table 1) and two of which were centered above the surface such that the bottom edge of the cold bubble was at the surface (bubbles ElevTall and ElevWide; Table 1). The various cold bubble shapes result in a range of turbulent behavior and therefore a range of cold pool evolutions. Additionally, the initial amplitude of each cold bubble was set to -5 K, -10 K, and -15 K for the 50 m and 100 m resolution tests. Only the -15 K amplitude was used for the 200 m and 400 m resolution tests because the cold pools in the coarser resolution simulations are much less turbulent, as will be shown in section 4. In total, 128 different simulations were performed, which are summarized in Table 1.

2.3. Analysis Methods

Since no background winds are included, the cold bubble initialization results in two identical cold pools propagating in opposite directions. Only the rightward moving cold pool is analyzed. Several different cold pool characteristics of interest are examined in this study. In this section, the various quantities used to analyze these characteristics are defined and explained.

The cold pool leading edge is identified by the largest gradient in θ at the lowest model level above ground. The identified cold pool edge is then used to calculate perturbation quantities (e.g., θ and pressure) in the cold pool relative to the mean environmental quantities ahead of the cold pool, hereafter called “cold pool perturbations.” The cold pool perturbations account for the changes that occur in the environment ahead of the cold pool in the ConsSHF simulations; such changes are not represented in perturbation quantities from the time-invariant base state. Therefore, the base state perturbations and cold pool perturbations are identical for the NoSHF and BulkSHF simulations, but they are not the same for the ConsSHF simulations.

For each grid column, the top of the cold pool is defined by the highest altitude of the -0.005 m s^{-2} thermal buoyancy contour, where the buoyancy threshold is the same as that used in T01 (different buoyancy thresholds were also tested and they did not change the results), and the thermal buoyancy [Doswell and Markowski, 2004] is calculated from the cold pool θ perturbation. The cold pool intensity C , or theoretical cold pool speed, is calculated for each grid column using the following equation [e.g., Benjamin, 1968; Rotunno et al., 1988]:

$$C^2 = 2 \int_0^H -g \frac{\theta'}{\theta_{\text{env}}} dz \quad (2)$$

where H is the height of the cold pool, g is the gravitational acceleration, and θ' is the cold pool perturbation relative to the mean θ ahead of the cold pool, θ_{env} . Noncold pool air is simply all air located above the identified cold pool top. Maximum vertical velocity is found within noncold pool air, and within 10 km of the cold pool's leading edge, in order to quantify the strength of the cold pool-driven ascent within environmental air that would be most favorable for convective initiation. An average cold pool propagation speed toward the end of the simulations is calculated from the distance traveled by the cold pool's leading edge over the last 1000 s. All other temporally averaged quantities exclude the first 1000 s to avoid the cold pool spin-up period and the influence of the initial conditions.

3. Results From the 50 m Simulations

3.1. Characteristics of the NoSHF-50 m Experiments

Figure 2 demonstrates the main features of one of the cold pools in the highest resolution experiments. The cold pool has taken on a classic shape with a shallow tail region and a 2 km deep head region. The strongest θ perturbations are located at the surface throughout ~ 5 km behind the leading edge of the cold pool (Figure 2c), and the strongest surface winds are located behind the strongest θ perturbations (Figure 2a). A broad and deep region of ascent is located above the cold pool head (Figure 2b), the magnitude of which is in keeping with previously observed gust front vertical velocity measurements of nearly 10 m s^{-1} [Martner, 1997]. Kelvin-Helmholtz (KH) waves are clearly evident in the θ and wind fields and are a result of shearing instability associated with the circulation induced by the cold pool. The KH waves are associated

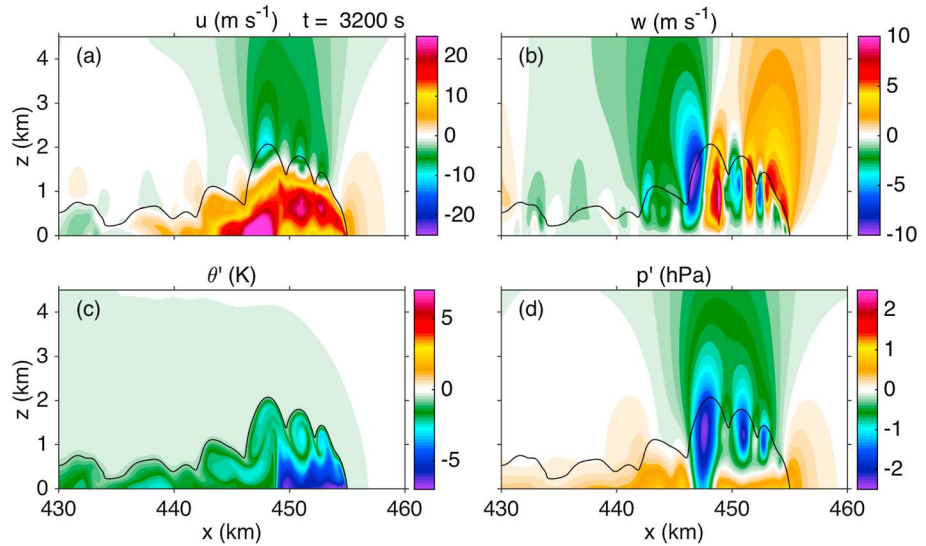


Figure 2. Cross sections of (a) zonal wind, (b) vertical velocity, (c) perturbation θ , and (d) perturbation pressure for simulation NoSHF-50m-SfcTall-15 at 3200 s. The -0.5 K perturbation θ is contoured in black for reference.

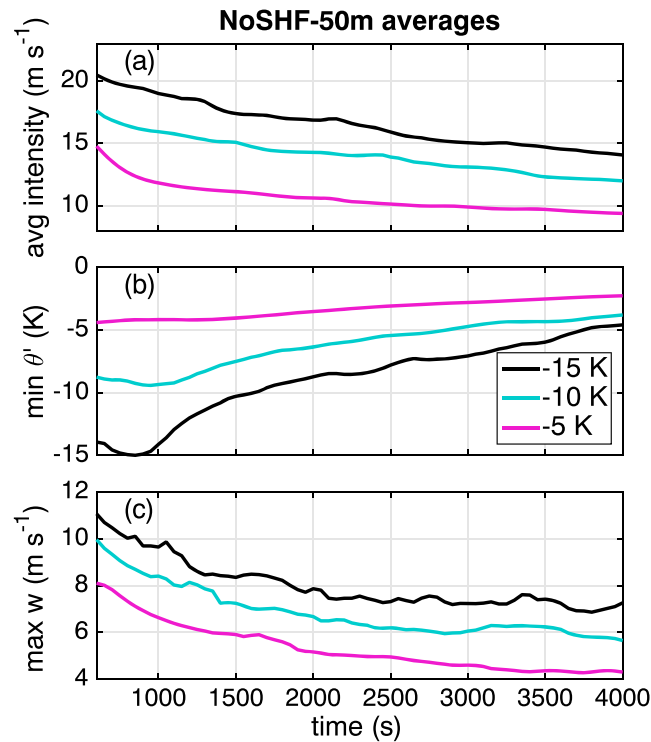


Figure 3. Time series of (a) cold pool intensity, (b) minimum cold pool perturbation, and (c) maximum vertical velocity in noncold pool air for the NoSHF-50m simulations. Results are averaged over the four initial cold bubble configurations (SfcTall, SfcWide, ElevTall, and ElevWide) for each of the three initial cold bubble amplitudes as indicated in the legend. The cold pool leading edge, cold pool intensity, and noncold pool air are determined as described in section 2.3. The cold pool intensity is averaged over 10 km behind the cold pool's leading edge in order to average over a consistent distance in all simulations and to incorporate the entire head region in the average.

with substantial fluctuations in the wind field within the cold pool itself and low-pressure perturbations at their center where the circulation is strongest (Figure 2d). Such KH waves have been noted in numerous other numerical simulations of density currents [DW87; Straka *et al.*, 1993; Xu *et al.*, 1996; Xue, 2002], as well as in observations of gust fronts, sea breezes, and bow echoes [Mueller and Carbone, 1987; Ralph *et al.*, 1993; Lapworth, 2000; Plant and Keith, 2007; Wakimoto *et al.*, 2006, Figure 16].

The evolution of several averaged cold pool characteristics in the NoSHF-50m simulations is shown in Figure 3 for each of the three initial cold bubble amplitudes (-15 K, -10 K, and -5 K), and the average cold pool propagation speeds over the last 1000 s of the simulations are listed in the second column of Table 2. Three different measures of cold pool dissipation are shown for the following reasons. First, the cold pool intensity (Figure 3a), calculated from the formula given in equation (2), is arguably the best measure of the overall strength of the cold pool, since it accounts for the integrated buoyancy over the entire depth of the cold pool. It is most closely related to the surface pressure perturbation in the cold pool

Table 2. Average Cold Pool Propagation Speed^a in the 50 m Experiments

Initial Cold Bubble Amplitude (K)	NoSHF (m s ⁻¹)	BulkSHF Difference (%) ^b	ConsSHF-300 Difference (%) ^b	ConsSHF-BulkAvg Difference (%) ^b
-15	12.23	-4.1	-7.2	-4.2
-10	10.53	-1.9	-5.6	-0.6
-5	8.13	-2.0	-8.8	-0.5

^aCold pool propagation speed over the last 1000 s for each individual simulation was determined by tracking the cold pool's leading edge as described in section 2.3. The propagation speeds were then averaged over the four initial cold bubble configurations (SfcTall, SfcWide, ElevTall, and ElevWide) for each of the three initial cold bubble amplitudes.
^bPercent differences in average cold pool propagation speed from NoSHF.

head and therefore to the cold pool propagation speed. In fact, the actual cold pool speeds calculated over the last 1000 s (Table 2) match the theoretical cold pool speeds shown in Figure 3a quite well, being only ~15% smaller. The cold pool intensity can be calculated in observational studies if high spatial resolution rawinsonde data are available from field campaign measurements, as was done for midlatitude squall line cold pools in *Bryan et al.* [2005] and *Bryan and Parker* [2010]. However, in most observational studies, buoyancy calculations throughout the cold pool depth are not possible due to the limited availability of rawinsonde data. In these cases, the surface temperature perturbations in the cold pool,

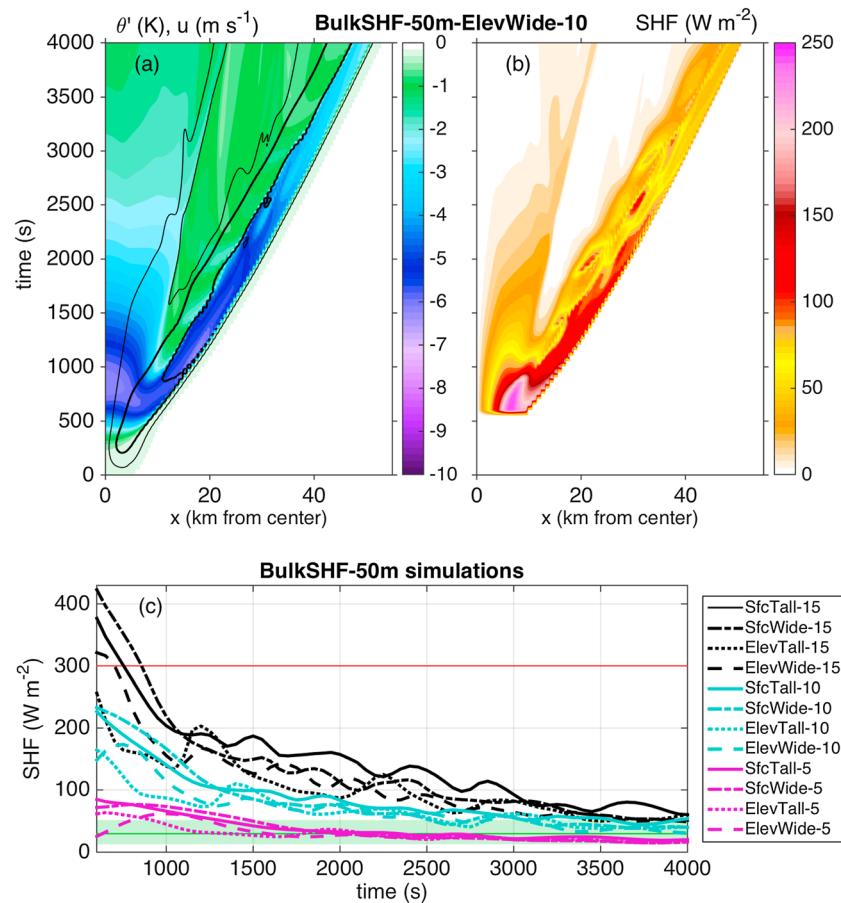


Figure 4. Hovmöller plot of (a) perturbation θ (shaded) and zonal wind ($5 m s^{-1}$ thin and $15 m s^{-1}$ thick black contours) at the lowest model level above ground (12.5 m) and (b) surface sensible heat flux for simulation BulkSHF-50 m-ElevWide-10. Note that the step-like patterns, such as near the cold pool's leading edge, are a result of the temporal output resolution of 50 s. (c) Time series of sensible heat flux averaged over 10 km behind the cold pool leading edge for each of the 12 BulkSHF-50 m simulations as indicated in the legend. The red line represents the SHF value for the ConsSHF-300 simulations, while the green line (shading) represents the median (minimum and maximum) SHF values used in the 12 ConsSHF-BulkAvg-50 m simulations.

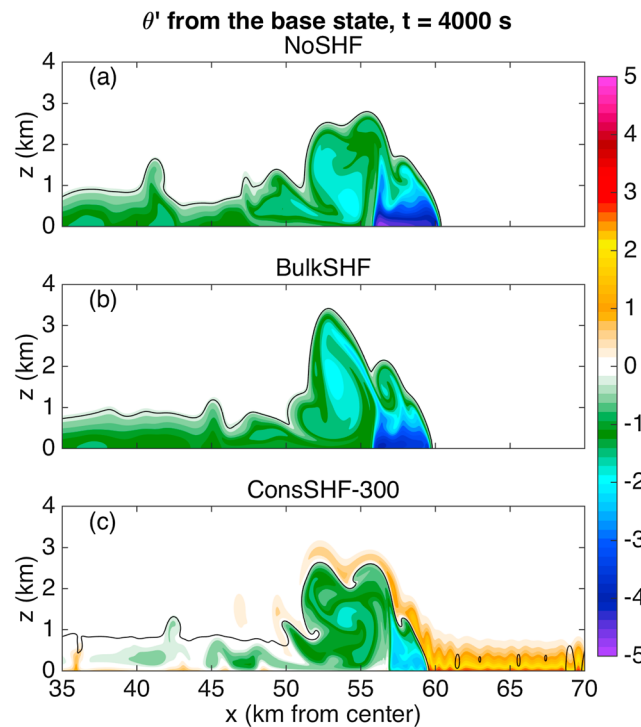


Figure 5. Cross sections of perturbation θ' relative to the base state (K) at 4000 s for the (a) NoSHF, (b) BulkSHF, and (c) ConsSHF-300 experiments in the 50m-ElevWide-15 simulation set. The -0.005 m s^{-2} buoyancy value is contoured in black.

~1500 s onward. As expected, the initially colder cold pools are stronger than the initially warmer cold pools throughout the simulation duration, and these colder cold pools also have 50% larger propagation speeds than the warmer cold pools (Table 2). Although the cold pools all dissipate at approximately the same rate in terms of their intensity (Figure 3a) and maximum vertical velocity (Figure 3c), the minimum θ' perturbations warm faster in the initially colder cold pools than in the initially warmer cold pools (Figure 3b). The minimum θ' perturbations, which are found at the surface, dissipate more quickly in the initially colder cold pools because the cold pool's internal circulation—which is stronger in the initially colder cold pools—acts to homogenize the vertical temperature distribution more rapidly through mixing.

3.2. SHF Modification of Cold Pool Characteristics

Before examining how SHFs influence the cold pools, the spatial and temporal bulk SHF patterns are first illustrated for one of the 50 m simulations (Figures 4a and 4b). In accordance with equation (1), SHFs are largest where the cold pool is coldest, directly behind the cold pool's leading edge, and where the wind speed is highest, 5–10 km behind the cold pool's leading edge. The oscillations in wind speed and SHFs that occur 5–10 km behind the leading edge of the cold pool from 1500 s onward are associated with the KH waves that cascade into the tail region of the cold pool (Figure 2). The impact of KH waves on near-surface fields behind the cold pool head has also been noted in observations [Mueller and Carbone, 1987; Ralph et al., 1993]. Although the range in SHFs is large among the 12 BulkSHF-50 m experiments during the first half of the simulations, the SHFs toward the end of the simulations are small in magnitude for all of the cold bubble experiments as the cold pool dissipates, as shown by the time series of BulkSHFs averaged over the cold pool head (Figure 4c). In other words, the SHFs in the initially stronger cold pools become similar to those in the initially weaker cold pools because the near-surface temperatures warm faster in the initially stronger cold pools, as shown in Figure 3b.

Potential temperature perturbations *relative to the time-invariant base state* for three of the SHF experiments at the end of one example set of cold pool simulations are shown in Figure 5. Several qualitative differences among the SHF experiments are evident that are also representative of the other simulation sets. Intuitively, the absolute cold pool temperatures are warmer with bulk and constant surface fluxes than without any

which are readily measurable by surface observation station networks, are sometimes used as a proxy for the strength of the cold pool, such as in Engerer et al. [2008]. Therefore, the minimum θ' perturbation is also shown here as another measure of the strength of the cold pool (Figure 3b). Third, maximum vertical velocity in noncold pool air (Figure 3c) is a good indicator of the potential for the cold pool to initiate new convection through mechanical lifting.

Figure 3 demonstrates that, even in the absence of SHFs, the cold pools slowly weaken or dissipate with time by all three measures of cold pool strength. For instance, the average cold pool intensities decrease by 20–25% between 1000 and 4000 s (Figure 3a). The cold pools without SHFs dissipate for two reasons. First, the cold air source is not maintained. Second, the cold pools are turbulent (Figure 2), and the KH waves help to entrain the warmer environmental air into the cold pool. The cold pools dissipate at relatively steady rates from

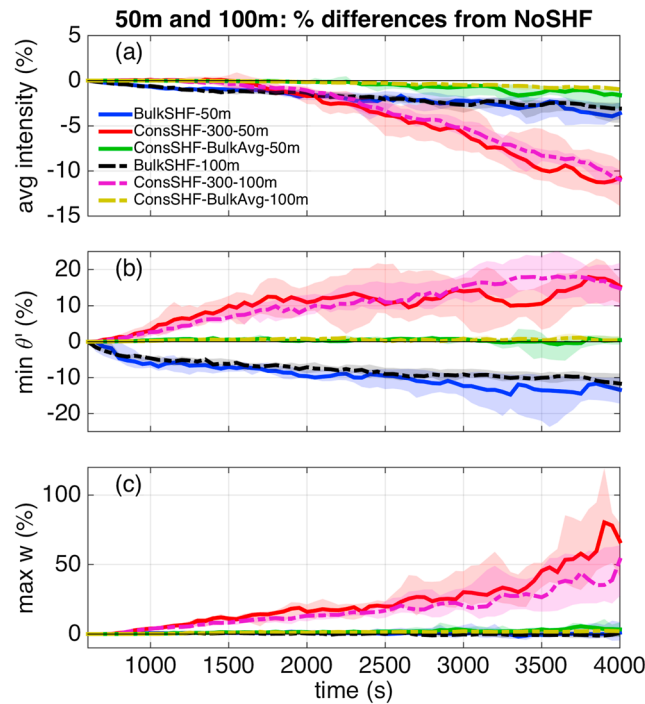


Figure 6. (a–c) Time series of the same quantities shown in Figure 3; recall that Figures 6a and 6b are calculated with cold pool perturbation quantities relative to the environment ahead of the cold pool (see section 2.3). For each of the 12 initial cold bubble simulations in the 50 m and 100 m resolution experiment sets, percent differences from NoSHF were calculated for BulkSHF, ConsSHF-300, and ConsSHF-BulkAvg; results are shown as percentiles (solid line: 50th percentile; shading: 25th and 75th percentiles). Note that in Figure 6b, since minimum θ perturbations are negative, a positive percent difference indicates that the minimum θ perturbation is colder.

initial cold bubble configurations (SfcTall, SfcWide, ElevTall, and ElevWide) and amplitudes (–15 K, –10 K, and –5 K) and hence the range in turbulent behaviors among the simulations. The average percent differences in cold pool propagation speed from the NoSHF simulations are also listed in Table 2. It is clear from Figure 6 and Table 2 that the way SHFs are represented has a significant impact on the *manner* in which the SHFs modify the cold pool characteristics. Specifically, while both bulk and constant SHFs weaken the cold pool intensity and hasten its dissipation relative to the NoSHF cases, the cold pool intensity is reduced by the largest percentage in the ConsSHF-300 cases (up to 10–15% weaker), by up to 5% in the BulkSHF cases, and by only a few percent in the ConsSHF-BulkAvg cases at the end of the simulations (Figure 6a). The cold pool propagation speeds are also reduced the most in the ConsSHF-300 simulations (Table 2) in keeping with the less negatively buoyant cold pools. However, if cold pool dissipation is measured in terms of the minimum cold pool θ perturbation (recall that the cold pool perturbations are calculated relative to the environment ahead of the cold pool), the ConsSHF-300 minimum θ perturbations are 10–20% *colder* (i.e., *stronger*), while the BulkSHF minimum θ perturbations are 10–20% *warmer* (i.e., *weaker*), relative to the NoSHF cases (Figure 6b), which is opposite to the cold pool intensity trends. Finally, while bulk SHFs and the smaller magnitude constant SHFs make very little difference in the maximum vertical velocities, the 300 W m^{–2} prescribed SHFs substantially increase the maximum vertical velocities by up to 50–100% (Figure 6c).

Exactly how then do SHFs modify the cold pool characteristics and influence cold pool dissipation, and why are the impacts of bulk versus constant SHFs on these characteristics so different? To answer these questions, temporally averaged cold pool properties for one set of SHF experiments are shown in Figures 7 and 8. Only one simulation set is shown for clarity. This simulation set is representative of the other simulation sets. The trends in cold pool characteristics for the bulk SHFs are discussed first and then the trends for the constant SHF cases are explained. In the following discussion, recall that cold pool perturbation quantities are

surface fluxes. The absolute temperatures have warmed significantly more in the ConstSHF-300 simulation than in the BulkSHF simulation because the specified 300 W m^{–2} SHF is greater in magnitude than the bulk SHFs throughout most of the simulation (Figure 4c). The cold pool and KH wave structure also appear different among the three simulations. Finally, the air ahead of the cold pool in the ConsSHF-300 simulation has become statically unstable as a result of the uniform surface heating and is evolving into individual convective plumes (Figure 5c). In other words, turbulent kinetic energy (TKE) is generated in the environment ahead of the cold pool. Some of this heated air is then lifted along the cold pool head, as is evident in Figure 5c.

The impacts of bulk and constant SHFs on the average cold pool intensity, minimum cold pool θ perturbation, and maximum vertical velocity in the 50 m experiments are quantified in Figure 6 (blue, red, and green lines; the 100 m results will be discussed in section 4). The shading indicates the variability in the percent differences of these quantities from the NoSHF-50 m simulations. This variability arises due to the different

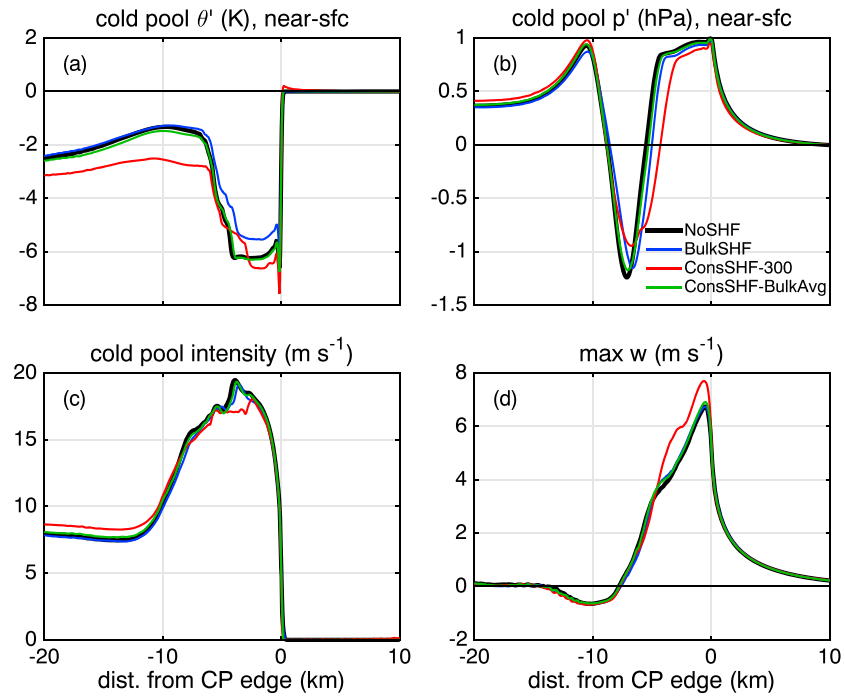


Figure 7. (a) Cold pool θ' perturbation and (b) cold pool pressure perturbation at the lowest model level above ground (12.5 m), (c) cold pool intensity, and (d) maximum vertical velocity in noncold pool air for the 50m-ElevWide-15 experiment set. All quantities are first subset relative to the cold pool leading edge and then temporally averaged between 1000 and 4000 s as described in section 2.3. Cold pool perturbations are relative to the environment ahead of the cold pool.

calculated relative to the environment ahead of the cold pool, which are not necessarily the same as the perturbations relative to the time-invariant model base state shown in Figure 5 (see section 2.3).

In the bulk SHF cases, the near-surface cold pool θ' perturbations within 10 km behind the cold pool's leading edge are 10–20% warmer in BulkSHF than in NoSHF (Figure 7a) where the bulk SHFs are large

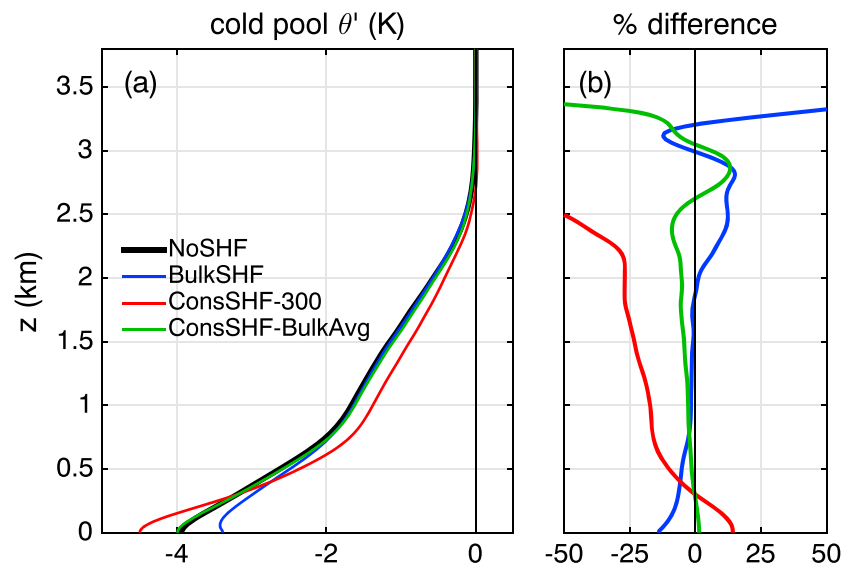


Figure 8. Profiles of (a) cold pool θ' perturbation relative to the environment ahead of the cold pool and (b) percent differences from NoSHF, averaged over 10 km behind the cold pool leading edge and temporally between 1000 and 4000 s, for the 50m-ElevWide-15 experiment set.

(Figure 4b). However, in the tail region where the bulk SHFs are small, the θ perturbations are nearly the same as NoSHF. The average cold pool θ perturbations are also warmer throughout the lowest 2 km of the cold pool head region and are warmest at the surface by nearly 15% in BulkSHF, as shown by the θ perturbation profiles in Figure 8. The high-pressure perturbations behind the leading edge of the cold pool and the integrated buoyancy are therefore also weaker (Figures 7b and 7c), and the propagation speed is slower in the BulkSHF cases (Table 2). (Note that the low-pressure perturbations from 5 to 10 km behind the cold pool edge are related to the KH wave circulations and hence are nonhydrostatic; see Figure 2.) However, the pressure and intensity changes are only 5% or less, and the vertical velocity in noncold pool air is nearly the same (Figure 7d). Thus, while the impact of bulk SHFs is significant on the near-surface temperature field, their impacts on the broad cold pool characteristics are not as large.

In the ConsSHF-300 case, Figure 7a demonstrates that the near-surface cold pool θ perturbations are, counter intuitively, colder than those in NoSHF by up to 10% in the head region and up to 100% in the tail region, as first shown in Figure 6b. While the cold pool intensity in the tail region is also stronger by about 10% in ConsSHF-300 (Figure 7c), in agreement with the temperature perturbation trends there, the intensity is weaker in the head region of the cold pool, which is opposite to the near-surface temperature perturbation trends in the cold pool head. *Bryan et al.* [2005] have also shown that cold pool intensity is not always well correlated with the surface temperature perturbations due to variations in stratification within the environment and the cold pool, and that caution must be exercised when using surface temperature perturbations to characterize the strength of cold pools. As expected, the cold pool pressure perturbation trends correspond to the intensity trends (Figure 7b) because pressure perturbations are hydrostatically related to the integrated buoyancy. The weaker pressure perturbations near the cold pool's leading edge result in slower propagation speeds (Table 2). The ConsSHF-BulkAvg simulations exhibit the same trends as the ConsSHF-300 cases but with much smaller magnitudes.

The reason for the opposite trend in the near-surface cold pool θ perturbation and the cold pool intensity in the ConsSHF cases is elucidated by the θ perturbation profiles (Figure 8) and the recollection that cold pool perturbations are calculated relative to the environment ahead of the advancing cold pool. Although *near-surface* cold pool θ perturbations in ConsSHF-300 are colder than those in NoSHF by nearly 15%, the θ perturbations above 0.3 km are warmer, by greater than 25% above 1.7 km (Figure 8b). (Again, the ConsSHF-BulkAvg results have the same trends as ConsSHF-300 but with smaller magnitudes.) This result can be understood by keeping in mind that both the cold pool and the environment ahead of the cold pool are heated at equal rates in the ConsSHF cases. The heating within the cold pool is vertically mixed and communicated throughout the cold pool due to the cold pool's internal circulations. Therefore, in the ConsSHF simulations, the near-surface temperatures increase more quickly in the environment than they do in the cold pool. This results in a stronger near-surface temperature difference between the cold pool and the environment in the two ConsSHF cases compared with NoSHF. Conversely, the temperature difference between the cold pool and the environment is weaker aloft where the environmental air is not directly heated by the surface. Also, as noted in the discussion of Figure 5, TKE is generated in the environment ahead of the cold pool in the ConsSHF simulations as the air becomes statically unstable near the surface, and this positively buoyant air is more easily lifted by the cold pool head. Aside from increasing the vertical velocities in noncold pool air by several m s^{-1} (Figures 7d and 6c), Figure 5 demonstrates that some of this heated environmental air is entrained into the cold pool head by the turbulent KH waves. This process also contributes to the warmer θ perturbations aloft in the ConsSHF cold pools through sensible heat flux convergence. Such heating by breaking KH waves was also shown to contribute significantly to the turbulent erosion of valley-trapped cold air pools within high-resolution 3-D simulations by *Lareau and Horel* [2015].

To summarize the ConsSHF results, when prescribed SHFs are included, the cold pool intensity is reduced, but near-surface cold pool temperature perturbations are enhanced, compared to when SHFs are excluded. These trends result from the heating of the environmental near-surface air ahead of the cold pool and subsequent entrainment of this heated air into the cold pool. Overall, SHFs can exert a significant influence on various cold pool characteristics, but the *manner* in which they do so strongly depends on the SHF formulation, the SHF magnitude, and the detailed flow structure within the cold pool.

3.3. Discussion

We ask two final questions based on these results: (1) what are the most important physical mechanisms for cold pool dissipation and (2) are proper representations of SHFs important to accurately capture cold pool dissipation, lifetimes, and the potential ability of the cold pool to initiate convection in cloud-resolving models? It should be noted that, with respect to question (1), the 2-D nature of our simulations makes it inappropriate to quantify the cold pool dissipation rates directly [e.g., *Tompkins, 2000*]. Rather, our goal is to compare the relative importance of the mechanisms that contribute to cold pool dissipation.

The ConsSHF experiments allow us to specifically explore how SHFs impact turbulence and entrainment into the cold pool, such as was done in *Linden and Simpson [1986]*, because the prescribed SHFs are the same everywhere and hence the cold pool is not heated *relative* to the environment (i.e., any more or less than the environment). Conversely, the BulkSHF experiments represent how SHFs directly modify the cold pool buoyancy through surface heating, as was investigated by *Ross et al. [2004]*, since these SHFs *only* occur within the cold pool (i.e., the environment ahead of the cold pool remains undisturbed, and hence, no bulk SHFs occur there). As discussed in section 3.1, the cold pool intensity weakens by 20–25% over 3000 s irrespective of whether SHFs are included, but bulk SHFs decrease cold pool intensities by at most an additional 5% (Figure 6a). On the other hand, for realistic peak daytime SHFs of 300 W m^{-2} , the constant SHFs decrease cold pool intensities by an additional 10–15% relative to the NoSHF cases (Figure 6a). Therefore, comparing the dissipation rates in the NoSHF cases to the additional enhancements in the dissipation rates for the various SHF simulations, we conclude that *entrainment of environmental air into the cold pool is an important mechanism for cold pool dissipation*. Furthermore, for ambient SHFs representative of daytime continental values over a relatively dry land surface type, *the impact of SHFs on near-surface environmental static stability, and hence entrainment into the cold pool, plays a more significant role in cold pool evolution than does direct modification of the cold pool buoyancy by SHFs*. This statement is in keeping with the findings of *Linden and Simpson [1986]* that SHF impacts on turbulent entrainment into a laboratory density current were significant. It is contrary to the conjecture by T01, and the findings of *Ross et al. [2004]*, that direct modification of cold pool buoyancy by surface fluxes is important, although those studies investigated weak tropical oceanic cold pools for which ambient SHF magnitudes are much smaller than the 300 W m^{-2} value tested here, and latent heat fluxes—which also modify the cold pool buoyancy—are substantial. In fact, in our simulations, the impact of bulk SHFs is greater than or equal to that of constant SHFs when the total energy input is comparable (Figure 6 and Table 2; compare BulkSHF to ConsSHF-BulkAvg), even though neither has a large effect on these cold pools. The cold pools simulated in this study are deeper, colder, more intense, and likely more turbulent than tropical oceanic cold pools. These considerations suggest that direct modification of the cold pool buoyancy by SHFs may play a larger relative role than demonstrated here over tropical oceanic regions, where cold pools are smaller, weaker, and less turbulent and where ambient SHFs are weak.

Finally, it can be argued that both types of SHFs enhance the potential of the cold pool to initiate new convection. In the constant SHF cases, convective initiation is more likely given the increased vertical velocities. In the BulkSHF cases, the maximum vertical velocities are the same compared to the NoSHF cases (Figure 6c), but the cold pool θ perturbations are warmer by up to 20% (Figure 6b). Since some parcels entering a convective updraft are likely to originate from within the cold pool [e.g., *Droegemeier and Wilhelmson, 1985; Torri et al., 2015*], it can be argued that the less negatively buoyant cold pools—i.e., those subjected to bulk surface fluxes—are more likely to initiate convection than the cold pools unmodified by SHFs, all else being equal. Therefore, the inclusion of SHFs and their impacts on both the near-surface stability and the cold pool buoyancy may impact the timing of cold pool-induced convective initiation.

Several assumptions used in our experiments will influence how these results translate to less idealized scenarios. First, the BulkSHF simulations presented here used a fixed surface temperature approximation, meaning that the bulk SHFs are only one-way interactive. A fully interactive land surface model will include variable land surface temperatures. It is possible that the cooling of the land surface by the cold pool itself would be great enough to suppress SHFs behind the cold pool's leading edge, an effect that was suggested in simulations of convection near Darwin, Australia, by *Del Genio et al. [2012]*. If we were to account for the land surface cooling due to the presence of the cold pool, the magnitude of the SHF contribution to cold pool dissipation by direct heating would be even smaller than suggested here, reinforcing our conclusion that SHFs primarily modify cold pool dissipation through their indirect influence on turbulent entrainment rates

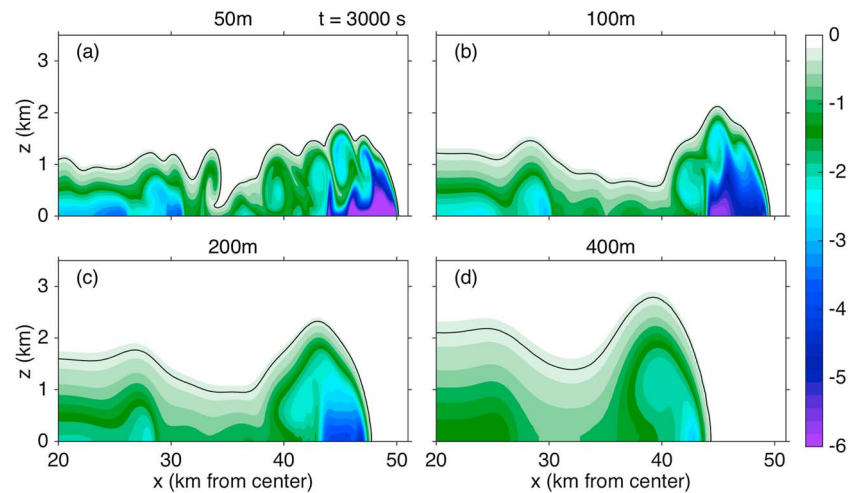


Figure 9. As in Figure 5 but for the NoSHF-SfcWide-15 simulations at 3000 s: (a) 50 m resolution, (b) 100 m resolution, (c) 200 m resolution, and (d) 400 m resolution.

in continental scenarios. Moreover, effects such as cloud cover or soil moisture heterogeneity will alter the net surface energy balance and change the SHFs ahead of the cold pool. This, in turn, will modify the magnitude of the SHF impacts on turbulent entrainment rates and sensible heat flux convergence into the cold pool. These effects will not be captured if specified surface fluxes are utilized. Prescribed surface fluxes are still common choices in modeling studies for various reasons. For instance, they are less computationally expensive than fully interactive land surface models, and prescribed fluxes are easy to constrain to observations—such as measured surface fluxes from field campaign data—or to impose as idealized, diurnally varying fluxes [e.g., *Khairoutdinov and Randall, 2006; Böing et al., 2012; Schlemmer and Hohenegger, 2014*]. However, our results demonstrating the importance of turbulent entrainment into the cold pool suggest that cloud-resolving model simulations utilizing surface fluxes determined by an interactive land surface model will be able to simulate cold pool characteristics and dissipation rates more accurately. This conclusion follows from the fact that the turbulent entrainment rates are dependent on the ambient SHF magnitudes, which can be highly variable.

Second, the 2-D diagnosis of entrainment rates will not be directly extendable to 3-D because the nature of the turbulent energy cascade is different in two and three dimensions [e.g., *Cantero et al., 2008; Bryan and Rotunno, 2014*]. However, since KH waves have been noted in numerous observations of cold pools [*Mueller and Carbone, 1987; Ralph et al., 1993; Wakimoto et al., 2006*] and in three-dimensional simulations [*Cantero et al., 2008*], we suspect that the qualitative results presented in this study can be extended to three dimensions. Additionally, since the breakdown of KH vortices into small-scale turbulence is better represented in three-dimensional simulations, the impacts of SHFs on entrainment into the cold pool may be even greater than demonstrated here.

4. Impact of Constant and Bulk SHFs for Coarser Resolutions

In this section, results from the coarser resolution experiment sets (Table 1) are investigated in order to assess whether the processes by which bulk and constant SHFs influence cold pool characteristics are also captured with coarser model resolutions. It is worth noting that the coarsest horizontal grid spacing of 400 m used in these tests is still considered to be very high resolution by today's standards for typical regional cloud-resolving modeling simulations.

Cross sections of θ perturbations at 3000 s for four NoSHF simulations with varying resolutions but identical initial cold bubble configurations are shown in Figure 9. It is evident from this figure that the cold pool minimum θ perturbations dissipate more quickly as the model resolution is coarsened; this is true of their intensity dissipation as well. They also have weaker vertical velocities by up to 30% (not shown) and slower propagation speeds. For instance, the average propagation speed among the four -15 K cold bubble simulations

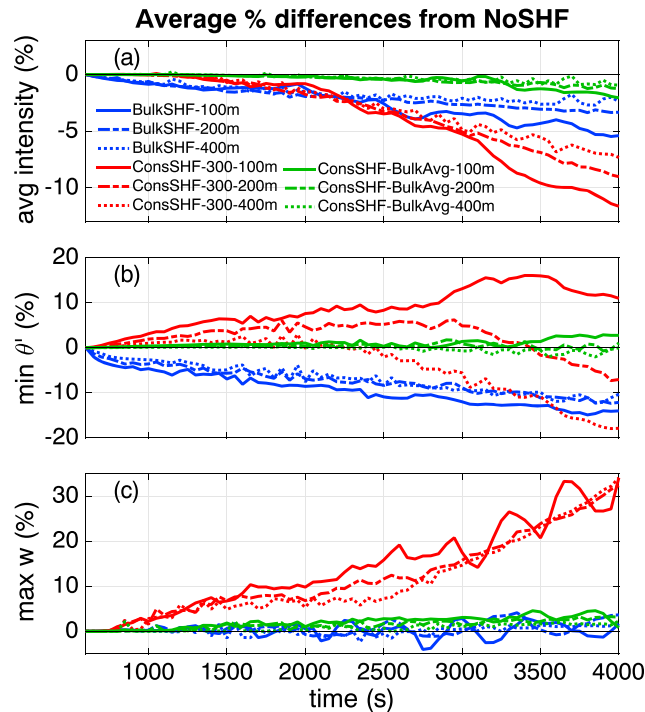


Figure 10. Time series of the same quantities shown in Figures 3 and 6. Percent differences from NoSHF were calculated for BulkSHF, ConsSHF-300, and ConsSHF-BulkAvg in each of the -15 K cold bubble amplitude experiments for the 100 m, 200 m, and 400 m resolution simulations. Results shown are averaged over the four initial cold bubble configurations for each of the resolution tests as indicated in the legend.

decreases by nearly 20% between the 50 m and 400 m experiment sets. Additionally, the coarser resolution simulations are less able to capture the detailed flow structure within and around the cold pool. The positively buoyant plumes of air that develop ahead of the cold pool in the ConsSHF-50 m simulations (Figure 5c) are not represented in any of the coarser resolution experiments (not shown). The KH waves, and therefore the internal flow structure within the cold pool, are less well resolved in the 100 m experiments than in the 50 m experiments, although the KH waves are clearly still present (Figure 9b). However, the KH waves are only marginally resolved at times in the 200 m experiments being barely evident in Figure 9c, and they are completely absent in the 400 m experiments (Figure 9d), in agreement with many previous studies [e.g., DW87; Straka et al., 1993; Bryan et al., 2003]. The 400 m experiments only capture the basic features of the cold pool structure, including the shallow tail region and the location of the coldest θ perturbations associated with the deeper head region.

Because even the 100 m simulations do not resolve the buoyant plumes—and hence the generation of ambient TKE—in the ConsSHF-300 experiments and do not capture the fine-scale details of the turbulent KH waves as well as in the 50 m simulations, there is less variability in the percent differences between the SHF and NoSHF cold pool characteristics in the 100 m experiments compared to the 50 m experiments, as indicated by the smaller spread in the 25th and 75th percentiles shown in Figure 6. Additionally, Figure 6 suggests that the magnitude of these percent differences generally decreases as the grid resolution is coarsened from the 50 m to the 100 m tests, which indicates that the cold pools are less sensitive to SHFs at coarser resolutions. Figure 10, which shows the trends in the same percent difference quantities that are shown in Figure 6 but which are now averaged over the four -15 K initial bubble simulations for the 100 m, 200 m, and 400 m resolution tests, reinforces this conclusion. For instance, the magnitudes of the percent decreases in the cold pool intensity are up to twice as large in the 100 m tests compared to the 400 m tests (Figure 10a). Moreover, the ConsSHF-300–200 m, ConsSHF-300–400 m, and ConsSHF-BulkAvg-400 m simulation sets actually have warmer, instead of colder, minimum θ perturbations relative to their respective NoSHF simulations (Figure 10b). This error is particularly severe in the ConsSHF-300–400 m simulations.

The cold pools are less sensitive to both bulk and constant SHFs as the resolution is coarsened for several reasons. First, although the computational smoothing rate is the same across the resolution experiments (see section 2.2), it is applied over a larger area as the grid spacing is increased. This means that the temperature perturbations and winds are ultimately smoothed out as the resolution is coarsened. As a result, the magnitude of the temperature perturbations and winds is weaker, and hence, the bulk SHF magnitudes are smaller, implying that their impacts on the cold pools are reduced. In the constant SHF cases, because the generation of positively buoyant plumes of air and TKE in the ambient environment is not captured and turbulent KH wave formation is not resolved, resulting sensible heat flux convergence into the cold pool is not adequately represented in the 200 m and 400 m results. Finally, due to the coarser vertical grid spacing, the heating ahead of the cold pool is distributed over a greater depth. Thus, the coarsest

resolutions incorrectly simulate a decrease, rather than an increase, in the near-surface cold pool temperature perturbation for the constant SHF cases.

From these resolution tests, we make the following recommendations. First, caution should be exercised when interpreting quantitative cold pool statistics obtained from simulations using horizontal (vertical) grid spacings coarser than 100 m (50 m), since cold pool characteristics like minimum θ perturbations can vary by more than a factor of 2 from their higher resolution counterparts. Second, where feasible, cloud-resolving modeling simulation results with 100 m or better grid spacings should be used to build cold pool parameterization schemes, particularly when incorporating the impacts of surface fluxes on cold pools. At coarser grid spacings, the cold pools are less sensitive to surface fluxes by up to a factor of 2 and some of the trends in cold pool characteristics *may even reverse*. Finally, future detailed process studies of cold pools and their interaction with deep convection should use horizontal and vertical grid spacings of 100 m and 50 m, respectively (or finer if possible), in order to adequately capture details of the cold pool evolution and its interaction with the environment. Although these recommendations have been made based on 2-D simulations and could vary with different subgrid diffusion parameterizations, they are in keeping with prior grid spacing recommendations to adequately simulate the largest turbulent eddies and their impacts on deep convection, based on 3-D simulations [Bryan *et al.*, 2003]. In fact, Bryan *et al.* [2003] suggested that even 125 m grid spacings might not be fine enough to adequately simulate the turbulent properties of cold pools in three dimensions (see their Figure 11).

5. Conclusions

The goals of this study have been to elucidate the mechanisms by which cold pools dissipate, the role of surface sensible heat fluxes (SHFs) on the dissipation rates, and the implications of this dissipation for convective initiation. These goals were accomplished with idealized, 2-D simulations of cold pools in which the effects of water vapor were excluded to isolate the SHFs from LHF. The environment was representative of cold pools that occur during the daytime over relatively dry continental surfaces. One hundred twenty-eight different simulations were performed. Three SHF formulations were tested: no SHFs, bulk SHFs that depend on the temperature and wind speed assuming a fixed surface temperature, and constant SHFs of (a) 300 W m^{-2} based on peak daytime SHFs from observations and (b) average SHF values from the bulk SHF simulations. The constant SHF cases represented the impacts of SHFs on turbulent entrainment into the cold pool because the SHF was the same everywhere, and therefore, the cold pool was not heated *relative* to the environment (i.e., the cold pool was not heated more or less than the environment outside of the cold pool). The bulk SHF experiments only included SHFs within the cold pool and therefore investigated how SHFs directly modify cold pool buoyancy through surface heating. Additionally, the relationships between cold pool characteristics and SHF formulations were investigated for different model resolutions with horizontal (vertical) grid spacings from 50 m (25 m) to 400 m (200 m).

In the highest resolution simulations, it was demonstrated that the inclusion of SHFs influences cold pool characteristics and cold pool dissipation rates, but the *manner* in which they do so strongly depends on the SHF formulation. Both bulk and constant SHFs hastened cold pool dissipation rates when assessed using the cold pool-integrated buoyancy and propagation speed, but the most significant changes in cold pool dissipation rates occurred for the constant 300 W m^{-2} SHF value. The bulk SHFs and the smaller magnitude constant SHFs computed from the averaged bulk SHFs had only slight impacts on cold pool dissipation. Additionally, while bulk SHFs reduced the *near-surface* cold pool temperature perturbations, constant SHFs enhanced the near-surface temperature differences between the cold pool and the environment because the constant SHFs heated the near-surface environmental air ahead of the cold pool more quickly than the cold pool air. These results suggest that the indirect impact of SHFs on entrainment into the cold pool is more important for cold pool dissipation than the direct modification of the cold pool buoyancy by SHFs for the SHF magnitudes and types of cold pools studied here. It was concluded that including the effects of sensible heating on cold pool dissipation may have implications for the timing of convective initiation through the SHF impacts on the near-surface environmental stability and on the cold pool's buoyancy. Finally, given the demonstrated importance of SHF impacts on turbulent entrainment into the cold pool, it was suggested that cloud-resolving model simulations will more accurately represent cold pool characteristics and their dissipation rates when using an interactive land surface model, which can capture variations in ambient SHFs and hence turbulent entrainment rates into the cold pool, compared with using prescribed surface fluxes.

The grid resolution experiments demonstrated that the detailed cold pool structure, flow, and turbulent development are not well captured as the grid spacings are systematically increased. As such, the simulated cold pools are less sensitive to SHFs under coarser resolutions. Moreover, the simulations with horizontal (vertical) grid spacings of 200 m (100 m) or greater not only poorly but sometimes wrongly represent the impacts of SHFs on the cold pool characteristics. It is recommended that future process studies of cold pools, especially those investigating the importance of surface fluxes, utilize horizontal (vertical) grid spacings of 100 m (50 m) or finer if we are to avoid such errors, and that cold pool parameterization schemes should be based on cloud-resolving model simulations with grid spacings of 100 m or better where feasible.

Future work should investigate the sensitivity of cold pool characteristics to surface fluxes under different stability regimes and wind shear profiles, which are known to have substantial influences on cold pool structure and propagation. The importance of environmental stability is highlighted in our constant SHF experiments, since the cold pool lifting of the near-surface statically unstable air produced substantially stronger vertical velocities near the cold pool head and enhanced warming of the cold pool air above the surface. The results presented here should be replicated in three-dimensional simulations as well. In addition to a more quantitative analysis of the cold pool dissipation rates themselves, lobe and cleft instabilities [e.g., Simpson, 1972] are possible in 3-D simulations and may contribute significantly to entrainment rates. Finally, observational studies of cold pools and surface fluxes would also be useful to assess the conclusions presented here. The opposite trends in near-surface cold pool temperatures and integrated cold pool buoyancy demonstrated in the constant SHF experiments highlight the critical need for more detailed observations of the full cold pool vertical structure.

Acknowledgments

The MODIS image in Figure 1 was obtained from the NASA LAADS Web Granule Browser (https://ladsweb.nas.nasa.gov/browse_images/granule_browser.html). The simulation data are available upon request from the authors (ldgrant@atmos.colostate.edu). This research has been supported by the National Science Foundation Graduate Research Fellowship Program under grant DGE-1321845 and by the Department of Energy under grant DE-SC0010569. The authors thank the three anonymous reviewers whose comments led to an improved manuscript.

References

- Benjamin, T. B. (1968), Gravity currents and related phenomena, *J. Fluid Mech.*, *31*(02), 209–248, doi:10.1017/S0022112068000133.
- Böing, S. J., H. J. J. Jonker, A. P. Siebesma, and W. W. Grabowski (2012), Influence of the subcloud layer on the development of a deep convective ensemble, *J. Atmos. Sci.*, *69*(9), 2682–2698, doi:10.1175/JAS-D-11-0317.1.
- Bryan, G., D. Ahijevych, C. Davis, S. Trier, and M. Weisman (2005), Observations of cold pool properties in mesoscale convective systems during BAMEX, in *11th Conf. on Mesoscale Processes*, vol. 61, JP5J, 12 pp., Am. Meteorol. Soc., Albuquerque, NM.
- Bryan, G. H., and M. D. Parker (2010), Observations of a squall line and its near environment using high-frequency rawinsonde launches during VORTEX2, *Mon. Weather Rev.*, *138*(11), 4076–4097, doi:10.1175/2010MWR3359.1.
- Bryan, G. H., and R. Rotunno (2014), Gravity currents in confined channels with environmental shear, *J. Atmos. Sci.*, *71*(3), 1121–1142, doi:10.1175/JAS-D-13-0157.1.
- Bryan, G. H., J. C. Wyngaard, and J. M. Fritsch (2003), Resolution requirements for the simulation of deep moist convection, *Mon. Weather Rev.*, *131*(10), 2394–2416, doi:10.1175/1520-0493(2003)131<2394:RRFTSO>2.0.CO;2.
- Cantero, M. I., S. Balachandrar, M. H. Garcia, and D. Bock (2008), Turbulent structures in planar gravity currents and their influence on the flow dynamics, *J. Geophys. Res.*, *113*, C08018, doi:10.1029/2007JC004645.
- Carbone, R. E., J. W. Wilson, T. D. Keenan, and J. M. Hacker (2000), Tropical island convection in the absence of significant topography. Part I: Life cycle of diurnally forced convection, *Mon. Weather Rev.*, *128*(10), 3459–3480, doi:10.1175/1520-0493(2000)128<3459:TICITA>2.0.CO;2.
- Dawson, D. T., M. Xue, J. A. Milbrandt, and M. K. Yau (2010), Comparison of evaporation and cold pool development between single-moment and multimoment bulk microphysics schemes in idealized simulations of tornadic thunderstorms, *Mon. Weather Rev.*, *138*(4), 1152–1171, doi:10.1175/2009MWR2956.1.
- Deardorff, J. W. (1972), Numerical investigation of neutral and unstable planetary boundary layers, *J. Atmos. Sci.*, *29*(1), 91–115, doi:10.1175/1520-0469(1972)029<0091:NIONAU>2.0.CO;2.
- Del Genio, A. D., J. Wu, and Y. Chen (2012), Characteristics of mesoscale organization in WRF simulations of convection during TWP-ICE, *J. Clim.*, *25*(17), 5666–5688, doi:10.1175/JCLI-D-11-00422.1.
- Doswell, C. A., and P. M. Markowski (2004), Is buoyancy a relative quantity?, *Mon. Weather Rev.*, *132*(4), 853–863, doi:10.1175/1520-0493(2004)132<0853:IBARQ>2.0.CO;2.
- Droegemeier, K. K., and R. B. Wilhelmson (1985), Three-dimensional numerical modeling of convection produced by interacting thunderstorm outflows. Part I: Control simulation and low-level moisture variations, *J. Atmos. Sci.*, *42*(22), 2381–2403, doi:10.1175/1520-0469(1985)042<2381:TDNMOC>2.0.CO;2.
- Droegemeier, K. K., and R. B. Wilhelmson (1987), Numerical simulation of thunderstorm outflow dynamics. Part I: Outflow sensitivity experiments and turbulence dynamics, *J. Atmos. Sci.*, *44*(8), 1180–1210, doi:10.1175/1520-0469(1987)044<1180:NSOTOD>2.0.CO;2.
- Enger, N. A., D. J. Stensrud, and M. C. Coniglio (2008), Surface characteristics of observed cold pools, *Mon. Weather Rev.*, *136*(12), 4839–4849, doi:10.1175/2008MWR2528.1.
- Garcia-Carreras, L., J. H. Marsham, D. J. Parker, C. L. Bain, S. Milton, A. Saci, M. Salah-Ferroudj, B. Ouchene, and R. Washington (2013), The impact of convective cold pool outflows on model biases in the Sahara, *Geophys. Res. Lett.*, *40*, 1647–1652, doi:10.1002/grl.50239.
- Gilmore, M. S., J. M. Straka, and E. N. Rasmussen (2004), Precipitation and evolution sensitivity in simulated deep convective storms: Comparisons between liquid-only and simple ice and liquid phase microphysics, *Mon. Weather Rev.*, *132*(8), 1897–1916, doi:10.1175/1520-0493(2004)132<1897:PAESIS>2.0.CO;2.
- Grant, L. D., and S. C. van den Heever (2014), Aerosol-cloud-land surface interactions within tropical sea breeze convection, *J. Geophys. Res. Atmos.*, *119*, 8340–8361, doi:10.1002/2014JD021912.
- Hartmann, D. L. (1994), *Global Physical Climatology*, Academic Press, San Diego, Calif.

- Jabouille, P., J. L. Redelsperger, and J. P. Lafore (1996), Modification of surface fluxes by atmospheric convection in the TOGA COARE region, *Mon. Weather Rev.*, *124*(5), 816–837, doi:10.1175/1520-0493(1996)124<0816:MOSFBA>2.0.CO;2.
- Johnson, R. H., and M. E. Nicholls (1983), A composite analysis of the boundary layer accompanying a tropical squall line, *Mon. Weather Rev.*, *111*(2), 308–319, doi:10.1175/1520-0493(1983)111<0308:ACAOTB>2.0.CO;2.
- Khairoutdinov, M., and D. Randall (2006), High-resolution simulation of shallow-to-deep convection transition over land, *J. Atmos. Sci.*, *63*(12), 3421–3436, doi:10.1175/JAS3810.1.
- Kingsmill, D. E. (1995), Convection initiation associated with a sea-breeze front, a gust front, and their collision, *Mon. Weather Rev.*, *123*(10), 2913–2933, doi:10.1175/1520-0493(1995)123<2913:CIAWAS>2.0.CO;2.
- Klemp, J. B., and R. B. Wilhelmson (1978), The simulation of three-dimensional convective storm dynamics, *J. Atmos. Sci.*, *35*(6), 1070–1096, doi:10.1175/1520-0469(1978)035<1070:TSOTDC>2.0.CO;2.
- Lapworth, A. (2000), Observations of atmospheric density currents using a tethered balloon-borne turbulence probe system, *Q. J. R. Meteorol. Soc.*, *126*(569), 2811–2850, doi:10.1002/qj.49712656911.
- Lareau, N. P., and J. D. Horel (2015), Turbulent erosion of persistent cold-air pools: Numerical simulations, *J. Atmos. Sci.*, *72*(4), 1409–1427, doi:10.1175/JAS-D-14-0173.1.
- Linden, P. F., and J. E. Simpson (1986), Gravity-driven flows in a turbulent fluid, *J. Fluid Mech.*, *172*, 481–497, doi:10.1017/S0022112086001829.
- Liu, C., and M. W. Moncrieff (1996), A numerical study of the effects of ambient flow and shear on density currents, *Mon. Weather Rev.*, *124*(10), 2282–2303, doi:10.1175/1520-0493(1996)124<2282:ANSOTE>2.0.CO;2.
- Liu, C., and M. W. Moncrieff (2000), Simulated density currents in idealized stratified environments, *Mon. Weather Rev.*, *128*(5), 1420–1437, doi:10.1175/1520-0493(2000)128<1420:SDCIIS>2.0.CO;2.
- Mallet, M., P. Tulet, D. Serça, F. Solmon, O. Dubovik, J. Pelon, V. Pont, and O. Thouren (2009), Impact of dust aerosols on the radiative budget, surface heat fluxes, heating rate profiles and convective activity over West Africa during March 2006, *Atmos. Chem. Phys.*, *9*(18), 7143–7160, doi:10.5194/acpd-9-2967-2009.
- Marshall, J. H., et al. (2013), Meteorology and dust in the central Sahara: Observations from Fennec supersite-1 during the June 2011 Intensive Observation Period, *J. Geophys. Res. Atmos.*, *118*, 4069–4089, doi:10.1002/jgrd.50211.
- Martner, B. E. (1997), Vertical velocities in a thunderstorm gust front and outflow, *J. Appl. Meteorol.*, *36*(5), 615–622, doi:10.1175/1520-0450(1997)036<0615:VVIATG>2.0.CO;2.
- Miller, S. D., A. P. Kuciauskas, M. Liu, Q. Ji, J. S. Reid, D. W. Breed, A. L. Walker, and A. Al Mandoos (2008), Haboob dust storms of the southern Arabian Peninsula, *J. Geophys. Res.*, *113*, D01202, doi:10.1029/2007JD008550.
- Mueller, C. K., and R. E. Carbone (1987), Dynamics of a thunderstorm outflow, *J. Atmos. Sci.*, *44*(15), 1879–1898, doi:10.1175/1520-0469(1987)044<1879:DOATO>2.0.CO;2.
- Plant, R. S., and G. J. Keith (2007), Occurrence of Kelvin-Helmholtz billows in sea-breeze circulations, *Boundary Layer Meteorol.*, *122*(1), 1–15, doi:10.1007/s10546-006-9089-x.
- Purdum, J. F. W. (1982), Subjective interpretation of geostationary satellite data for nowcasting, in *Nowcasting*, edited by K. Browning, pp. 149–166, Academic Press, London, U. K.
- Ralph, F. M., C. Mazaudier, M. Crochet, and S. V. Venkateswaran (1993), Doppler sodar and radar wind-profiler observations of gravity-wave activity associated with a gravity current, *Mon. Weather Rev.*, *121*(2), 444–463, doi:10.1175/1520-0493(1993)121<0444:DSARWP>2.0.CO;2.
- Rauber, R. M., et al. (2007), Rain in shallow cumulus over the ocean: The RICO campaign, *Bull. Am. Meteorol. Soc.*, *88*(12), 1912–1928, doi:10.1175/BAMS-88-12-1912.
- Rooney, G. G. (2015), Descent and spread of negatively buoyant thermals, *J. Fluid Mech.*, *780*, 457–479, doi:10.1017/jfm.2015.484.
- Ross, A. N., A. M. Tompkins, and D. J. Parker (2004), Simple models of the role of surface fluxes in convective cold pool evolution, *J. Atmos. Sci.*, *61*(13), 1582–1595, doi:10.1175/1520-0469(2004)061<1582:SMOTRO>2.0.CO;2.
- Rotunno, R., J. B. Klemp, and M. L. Weisman (1988), A theory for strong, long-lived squall lines, *J. Atmos. Sci.*, *45*(3), 463–485, doi:10.1175/1520-0469(1988)045<0463:ATFSL>2.0.CO;2.
- Schlemmer, L., and C. Hohenegger (2014), The formation of wider and deeper clouds as a result of cold-pool dynamics, *J. Atmos. Sci.*, *71*(8), 2842–2858, doi:10.1175/JAS-D-13-0170.1.
- Seigel, R. B., and S. C. van den Heever (2012), Simulated density currents beneath embedded stratified layers, *J. Atmos. Sci.*, *69*(7), 2192–2200, doi:10.1175/JAS-D-11-0255.1.
- Simpson, J. E. (1972), Effects of the lower boundary on the head of a gravity current, *J. Fluid Mech.*, *53*(04), 759–768, doi:10.1017/S0022112072000461.
- Smagorinsky, J. (1963), General circulation experiments with the primitive equations. I. The basic experiment, *Mon. Weather Rev.*, *91*(3), 99–164, doi:10.1175/1520-0493(1963)091<0099:GCEWTP>2.3.CO;2.
- Straka, J. M., R. B. Wilhelmson, L. J. Wicker, J. R. Anderson, and K. K. Droegemeier (1993), Numerical solutions of a non-linear density current: A benchmark solution and comparisons, *Int. J. Numer. Methods Fluids*, *17*(1), 1–22, doi:10.1002/flid.1650170103.
- Terai, C. R., and R. Wood (2013), Aircraft observations of cold pools under marine stratocumulus, *Atmos. Chem. Phys.*, *13*(19), 9899–9914, doi:10.5194/acp-13-9899-2013.
- Tompkins, A. M. (2000), The impact of dimensionality on long-term cloud-resolving model simulations, *Mon. Weather Rev.*, *128*(5), 1521–1535, doi:10.1175/1520-0493(2000)128<1521:TIODOL>2.0.CO;2.
- Tompkins, A. M. (2001), Organization of tropical convection in low vertical wind shears: The role of cold pools, *J. Atmos. Sci.*, *58*(13), 1650–1672, doi:10.1175/1520-0469(2001)058<1650:OOTCIL>2.0.CO;2.
- Torri, G., Z. Kuang, and Y. Tian (2015), Mechanisms for convection triggering by cold pools, *Geophys. Res. Lett.*, *42*, 1943–1950, doi:10.1002/2015GL063227.
- van den Heever, S. C., and W. R. Cotton (2004), The impact of hail size on simulated supercell storms, *J. Atmos. Sci.*, *61*(13), 1596–1609, doi:10.1175/1520-0469(2004)061<1596:TIOHSO>2.0.CO;2.
- Wakimoto, R. M., H. V. Murphey, A. Nester, D. P. Jorgensen, and N. T. Atkins (2006), High winds generated by bow echoes. Part I: Overview of the Omaha bow echo 5 July 2003 storm during BAMEX, *Mon. Weather Rev.*, *134*(10), 2793–2812, doi:10.1175/MWR3215.1.
- Wilhelmson, R. B., and C.-S. Chen (1982), A simulation of the development of successive cells along a cold outflow boundary, *J. Atmos. Sci.*, *39*(7), 1466–1483, doi:10.1175/1520-0469(1982)039<1466:ASOTDO>2.0.CO;2.
- Wilson, J. W., and W. E. Schreiber (1986), Initiation of convective storms at radar-observed boundary-layer convergence lines, *Mon. Weather Rev.*, *114*(12), 2516–2536, doi:10.1175/1520-0493(1986)114<2516:IOCSAR>2.0.CO;2.
- Wood, R., C. S. Bretherton, D. Leon, A. D. Clarke, P. Zuidema, G. Allen, and H. Coe (2011), An aircraft case study of the spatial transition from closed to open mesoscale cellular convection over the Southeast Pacific, *Atmos. Chem. Phys.*, *11*(5), 2341–2370, doi:10.5194/acp-11-2341-2011.

- Xu, Q. (1992), Density currents in shear flows—A two-fluid model, *J. Atmos. Sci.*, *49*(6), 511–524, doi:10.1175/1520-0469(1992)049<0511:DCISFA>2.0.CO;2.
- Xu, Q., M. Xue, and K. K. Droegemeier (1996), Numerical simulations of density currents in sheared environments within a vertically confined channel, *J. Atmos. Sci.*, *53*(5), 770–786, doi:10.1175/1520-0469(1996)053<0770:NSODCI>2.0.CO;2.
- Xue, M. (2002), Density currents in shear flows: Effects of rigid lid and cold-pool internal circulation, and application to squall line dynamics, *Q. J. R. Meteorol. Soc.*, *128*(579), 47–73, doi:10.1256/00359000260498789.
- Young, G. S., S. M. Perugini, and C. W. Fairall (1995), Convective wakes in the equatorial western Pacific during TOGA, *Mon. Weather Rev.*, *123*(1), 110–123, doi:10.1175/1520-0493(1995)123<0110:CWITEW>2.0.CO;2.
- Zuidema, P., Z. Li, R. J. Hill, L. Bariteau, B. Rilling, C. Fairall, W. A. Brewer, B. Albrecht, and J. Hare (2012), On trade wind cumulus cold pools, *J. Atmos. Sci.*, *69*(1), 258–280, doi:10.1175/JAS-D-11-0143.1.